New Polarimetric Data for the Galilean Satellites : Europa Observations and Modeling

Kiselev, Nikolai

2022-06-01

New Polarimetric Data for the Galilean Satellites: Europa Observations and Modeling

Nikolai Kiselev[1] , Vera Rosenbush[2,3], Karri Muinonen[4], Ludmilla Kolokolova[5] , Aleksandr Savushkin[1], and Nikolai Karpov[6]

[1] Crimean Astrophysical Observatory, Nauchnij, 298409 Crimea[†]; kiselevnn42@gmail.com
[2] Taras Shevchenko National University of Kyiv, Astronomical Observatory, 3 Observatorna Str., 04053 Kyiv, Ukraine
[3] Main Astronomical Observatory of the National Academy of Sciences of Ukraine, 27 Zabolotnoho Str., 03143 Kyiv, Ukraine
[4] University of Helsinki, Department of Physics, Helsinki, Finland
[5] University of Maryland, College Park, MD 20742, USA
[6] International Center for Astronomical, Medical and Ecological Research, Peak Terskol Observatory, Ukraine
Received 2022 February 10; revised 2022 April 27; accepted 2022 April 29; published 2022 June 6

Abstract

This paper is dedicated to a long-standing problem of the shape of the negative branch of polarization (NBP) for Jupiter's moon Europa, determination of which is crucial for the characterization of the icy regolith on this satellite and similar objects, as well as for further progress in understanding light scattering by particulate surfaces. To establish the shape of Europa's NBP, in 2018–2021 we accomplished high-precision disk-integrated polarimetry of Europa in the *UBVRI* bands using the identical two-channel photoelectric polarimeters mounted on the 2.6 m Shajn reflector of the Crimean Astrophysical Observatory and the 2 m telescope of the Peak Terskol Observatory. We found that the polarization dependence on the phase angle in each filter is an asymmetric curve with a sharp polarization minimum $P_{min} \approx -0.3\%$ at phase angle $\alpha_{min} \leqslant 0°.4$, after which the polarization degree gradually increases to positive values, passing the inversion angle at $\alpha_{inv} \approx 6° - 7°$. Within the error limits, the parameters P_{min}, α_{min}, and α_{inv} of the NPB are independent of the wavelength in the visible spectrum. The polarization curve clearly demonstrates the so-called polarization opposition effect (POE). Our analysis of the previous and new polarimetric observations of Europa allows us to conclude that the POE is caused by coherent backscattering of sunlight on microscopic icy grains covering Europa's surface. Computer modeling with the numerical radiative transfer coherent backscattering method demonstrates that the best fit to the polarimetric observations and geometric albedo of Europa is provided by a regolith layer of elementary single-scattering albedo $\sim$0.985 and extinction mean free path length $2\pi l/\lambda_{eff} \approx 150$, λ_{eff} representing the effective wavelength in the *UBVRI* spectral bands.

Unified Astronomy Thesaurus concepts: Jovian satellites (872); Galilean satellites (627); Europa (2189); Polarimetry (1278)

1. Introduction

1.1. Characterizing the Europa Surface

The surface of Europa is covered with a layer of ice with a complex pattern of cracks, discovered by the two Voyager missions in 1979, and a small number of impact craters. Moreover, these missions provided the first hint that Europa may contain liquid water. Recent ground-based and Hubble Space Telescope observations and a reanalysis of some data from the Galileo spacecraft have revealed thin plumes of water most likely ejected from the subsurface ocean. In 2019 November, plumes of water vapor above Europa's surface that may be venting into space from the icy crust itself were first directly detected with the spectral observations (Paganini et al. 2020). A cryovolcanic active area on the surface of Europa, probably also originating from the subsurface saline ocean, was detected by Cassen et al. (1979), Kivelson et al. (2000), Zimmer et al. (2000), and Sparks et al. (2016, 2017). These active phenomena can affect the surface characteristics. For

example, warmer liquid water below the ice layer may lead to the sintering of icy grains, modifying the surface texture (Poch et al. 2018).

Observations from the Galileo spacecraft revealed mineral salts on the surface of the satellite, indicating an interaction of the surface matter with the ocean of salty water. There are also signs of organic compounds and hydrogen peroxide, which is frozen in the ice. Europa's very thin atmosphere is composed mostly of oxygen and contains traces of water and hydrogen. Complex organic matter on the surface and subsurface ocean makes Europa one of the best candidates for extraterrestrial life in the solar system.

These results have renewed scientific interest in the study of Europa by both ground-based and space-based means, including the planned NASA Europa Clipper and ESA JUICE missions. The main goals of these missions are primarily to search for biosignatures in the subsurface, characterization of the composition of near-subsurface material, and determination of the proximity of liquid water and subsurface ocean.

The icy surface makes Europa one of the most reflective objects in the solar system; its geometric albedo in the *V* band is equal to 0.67. The light scattered by Europa shows an interesting phenomenon near opposition: a narrow photometric surge of brightness. The phase curves of brightness for the leading and trailing hemispheres of Europa's surface exhibit a sharp nonlinear increase in brightness, approaching the opposition at phase angles $\alpha \leqslant 2°$, that is superposed on a smooth photometric phase curve. This spike in the intensity of

---

the reflected light of Europa, the so-called brightness opposition effect (BOE), was detected by Thompson & Lockwood (1992) and Domingue et al. (1991). Using data from the Galileo mission, Helfenstein et al. (1998) confirmed the strong and very narrow BOE for Europa and studied it in detail.

Another interesting phenomenon is negative linear polarization at small phase angles. This means that the electric field vector component parallel to the scattering plane dominates the perpendicular component. The observed angular dependence of negative polarization for atmosphereless solar system bodies (ASSBs) and laboratory samples usually exhibits a negative polarization branch (NPB) that is almost parabolic with the minimum at approximately $5° - 15°$, depending on the properties of the scattering surface (Geake & Geake 1990; Shkuratov et al. 2002; Mishchenko et al. 2010; Bagnulo et al. 2011; Afanasiev et al. 2014; Levasseur-Regourd et al. 2015; Belskaya et al. 2017). However, in some cases a strongly asymmetric NPB with the minimum centered at about $0°.5–2°$ is observed. Lyot (1929) and Johnson et al. (1980) were the first to measure negative polarization for the A and B rings of Saturn before and after opposition within the range of phase angles $0°.5 - 6°$ and revealed that the phase curve of polarization was asymmetric with a minimum of -0.5% at a phase angle of about $3°$. The authors extrapolated sharp change of polarization at very small phase angles $0° < \alpha < 0°.5$ and called it "the hypothesized polarimetric opposition effect." Rosenbush et al. (1997, 2002) discovered the polarization minimum for a number of other high-albedo ASSBs, including the Jovian moon Europa. It should be noted that for Saturn's A and B rings a photometric opposition spike was also found (von Seeliger 1887; Müeller 1893; Franklin & Cook 1965).

Shkuratov (1985, 1991) and Muinonen (1990, 1994) suggested that coherent backscattering of sunlight by the regolith grains on the surfaces of ASSBs can be the universal physical mechanism for the photometric opposition effect, as well as for the negative branches of polarization. In particular, Muinonen (1990) and Muinonen et al. (1991) showed rigorously using the Maxwell equations that small particles close to interfaces give rise to coherent backscattering peaks in intensity and NPBs in the linear polarization for unpolarized incident light.

Mishchenko (1993) showed, for Saturn's rings, that both opposition phenomena, the BOE and a deep minimum of negative polarization, called the polarimetric opposition effect (POE), have a common origin and are caused by coherent backscattering of light by a layer composed of nonabsorbing or weakly absorbing sub-micrometer-sized grains. The angular semiwidth of both the photometric and polarization opposition effects should be approximately the same. This was confirmed by theoretical calculations of the full angular profiles of the intensity and polarization for nonabsorbing Rayleigh scatterers (Mishchenko et al. 2000).

Muinonen (2004) then provided the full radiative transfer coherent backscattering solution (RT-CB) for discrete random media of absorbing and nonabsorbing spherical scatterers (including the Rayleigh scatterers), with a strict and successful comparison against the reference results by Mishchenko et al. (2000). Later, Muinonen et al. (2012) used the RT-CB method to provide unequivocal proof that the coherent backscattering mechanism was indeed responsible for the backscattering peak and negative polarization computed rigorously using the superposition T-matrix method (STMM) based on the Maxwell equations for spherical discrete random media of spherical constituent particles (Mishchenko et al. 2007). Finally, the RT-CB method was extended to dense discrete random media of scatterers by Muinonen et al. (2018) and Markkanen et al. (2018), accounting exactly for near-field effects using the STMM.

In a number of papers (Mishchenko 1993; Rosenbush et al. 1997; Mishchenko et al. 2000; Muinonen et al. 2015) it was shown that an NPB near the backward scattering direction can take the shape of a deep minimum of negative polarization. The shape of the NPB and its characteristics (the degree of polarization at the minimum $P_{\min}$, the corresponding phase angle $\alpha_{\min}$, and the inversion angle α_{inv} at which polarization changes sign from negative to positive) are caused by various mechanisms of light scattering, and its specific shape is determined by the interaction of these mechanisms, depending on the properties of the scattering media. Note that the NPB shape can differ significantly even for objects of the same class owing to differences in the surface composition and structure.

1.2. Overview of Past Polarimetric Observations of Europa

Intensive polarimetric observations of Europa were carried out prior to the early 1990s (Veverka 1971; Gradie & Zellner 1973; Dollfus 1975; Veverka 1977; Zellner & Gradie (in Veverka 1977); Botvinova & Kucherov 1980; Bolkvadze 1981; Chigladze 1989). Unfortunately, with the exception of Chigladze's data, there had been no measurements of the polarization of this satellite at phase angles smaller than $2°$. Dollfus (1975) concluded that a change of sign of the polarization of Europa from positive to negative occurred near a phase angle of $\sim 9°$, remaining less than 0.1% (in absolute value) at smaller phase angles. The uncertainties in the data were within the range 0.03%–0.1%. The author assumed that the shape of the NPB for Europa was close to parabolic (see Figure 1 in Dollfus 1975) and there was no difference in polarization for the hemispheres of Europa. A very good agreement with the Dollfus data for Europa in the V band was obtained by Zellner & Gradie (see Figure 10.6 in Veverka 1977).

Botvinova & Kucherov (1980) for the first time observed the Galilean satellites in six spectral bands from 390 to 685 nm. These authors concluded that in the studied spectral range the degree of polarization for Europa, as well as for other Galilean satellites, is independent of wavelength.

Chigladze (1989) found that at phase angles smaller than $1°$ the polarization degree was positive for all four Galilean satellites. Later, Morozhenko (2001) found that the degree of polarization for Europa was $0.25\% \pm 0.02\%$ at a phase angle of $0°.46$, and the plane of polarization was not in the scattering plane or perpendicular to it, but forms the angle $\sim 45°$. Then, according to $P_r = P \cos 2\theta_r$, the corresponding value P_r was equal to 0.02%.

In 1988–1991, Rosenbush et al. (1997) performed the *UBVR* polarimetric observations of Europa in the range of phase angles from $0°.2$ to $11°.8$ and first detected a sharp minimum of negative polarization centered at a very small phase angle of $0°.6–0°.7$ and superposed on a wide, nearly parabolic NPB. However, these measurements were of low accuracy, and it was impossible to determine the shape of this peak and of the whole NPB.

Kiselev et al. (2009) carried out polarimetric observations of the Galilean satellites, as well as the north and south polar

regions of Jupiter, within the range of phase angles $0°.13–0°.62$. These observations confirmed the findings of Rosenbush et al. and showed that the results of Chigladze and Morozhenko obtained by them at phase angles $\alpha < 1°$ are erroneous owing to incorrect determination of the position angle of the scattering plane.

More accurate ($\sigma_p \approx 0.02\%–0.03\%$) measurements of the polarization of Europa within the range of phase angles $0°.2–2°.2$ were obtained in 2000 by Rosenbush & Kiselev (2005). The authors confirmed the existence of the sharp polarization minimum for Europa at phase angles smaller than $1°$. This minimum for Europa was also confirmed by Zaitsev (2016), who carried out the polarization measurements in the *UBVRI* filters at phase angles of $0°.14–11°.4$ during 2007–2014. Based on all available polarization measurements collected in the database Polarimetry of Planetary Satellites by Zaitsev et al. (2012a), the whole NPBs for Io, Europa, and Ganymede were presented in the form of the bimodal phase-angle dependences of polarization, which means overlap of the parabolic curve and the curve with a sharp narrow minimum (Rosenbush et al. 2015).

1.3. Objectives of This Study

A survey of the available observations showed that polarimetric observations of the Galilean satellites with high accuracy in different spectral bands in the opposition region ($\alpha \leqslant 2°$), as well as in the whole range of phase angles accessible for Jupiter satellites ($\alpha < 12°$), are extremely rare, and the behavior of the negative polarization, including its wavelength dependence, is still unknown in detail. Besides, there is a large scatter in the data obtained by different authors (see, e.g., Mishchenko et al. 2010; Rosenbush et al. 2015).

Therefore, the main objective of the present work was to obtain high-precision measurements of the polarization of the Galilean satellites in the whole range of accessible phase angles and in a wide spectral range. High-albedo satellites Io, Europa, and Ganymede, having rather different surface compositions, were selected for a careful study of their polarization near opposition and determining the exact shape of the POE. Note that for those objects the characteristics of the BOE are well known, which adds reliability to the interpretation of the polarimetric results.

In the present paper, we report the results of a long series of high-accuracy measurements of the polarization of Europa obtained at the 2.6 m telescope of the Crimean Astrophysical Observatory (CrAO) and the 2 m telescope of the Peak Terskol Observatory (PTO) with new polarimeters. The current program was started in 2018, and it is still ongoing. Here we present the results acquired for Europa, which allow us to constrain the physical properties of the regolith on its surface.

2. Observations, Instrumentation, and Data Reduction

We observed the Galilean satellites of Jupiter with the 2.6 m (F/16) Shajn telescope of the CrAO and with the 2 m (F/8) Ritchey–Chrétien–Coudé telescope of the International Center for Astronomical, Medical and Ecological Research for the measurements of their polarization during 2018–2021. The range of phase angles at which the observations were obtained extends from $0°.12$ to $11°.22$.

The telescopes are equipped with two-channel photoelectric polarimeters "POLSHAKH" (Shakhovskoy et al. 2022) of

identical design based on the principle of synchronous detection, which makes the polarization measurements almost independent of the weather conditions and ensures their high accuracy. In the red channels, the cooled photomultiplier tubes (PMTs) Hamamatsu R943-02 are used as detectors. These channels are used for observations of the objects in the *R* and *I* bands. The central wavelength/FWHM of the *R* filter at the CrAO polarimeter is 688/231 nm, while that at the PTO polarimeter is 683/159 nm. The central wavelength/FWHM of the *I* filter is 809/188 nm in both polarimeters. In the blue channels, the uncooled EMI 6556B PMTs are used, which provide observations in the $U(360/74$ nm), $B(434/117$ nm), and V (540/80 nm) bands.

The optical path of each polarimeter includes a modulator, which is a rapidly rotating achromatic wave plate ($\sim$30 rotations per second). There are two wave plates: a half-wave plate ($\lambda/2$ plate) for measurements of linear polarization, and a quarter-wave plate ($\lambda/4$ plate) for simultaneous measurements of linear and circular polarization. After the modulator, a Wollaston prism splits the incoming light into two orthogonally (ordinary O and extraordinary E) polarized beams, which then are separated by folding mirrors into two channels, so each can have its own set of spectral filters and detectors optimized for the desired wavelength. The rotation of the phase plate is synchronized with the PMT pulse counts, which are counted separately in each of the 16 sectors of the phase plate position $0° − 22°.5$, $22°.5–45°$, ... , $337°.5 − 360°$ for two orthogonally polarized beams. Further, we will consider the operation of the polarimeter in the linear polarization mode.

The intensity of light transmitted through a perfect quarter-wave phase plate with optical axis at position angle ϕ followed by an analyzer with the principal plane at position angle $\psi = 0°$ can be written according to Serkowsky (1974):

$$I(\phi) = \frac{1}{2}(1 + q\cos 4\phi + u\sin 4\phi). \tag{1}$$

This technique ensures quasi-simultaneous measurements of the Stokes parameters q and u of the incident light. The advantage of this method is independence of the measured polarization parameters of the changes in the incoming intensity caused by variability of the object and/or of the atmospheric extinction.

Specific features of measuring the sky background were that the background was measured before and after observation of the satellite from both sides and at equal distances in the direction perpendicular to the "planet–satellite" direction, following Lockwood (1983). It was corrected by interpolating the background counts to the middle time of the object observation. After the sky background correction, the solution of the system of Equations (1) for 16 positions of the quarter-wave phase plate allowed us to obtain the values of the Stokes parameters of the program object in the instrumental system q_{obs} and u_{obs} for each exposure. Based on entire series of observations of objects, the mean $\bar{q}_{obs}$ and $\bar{u}_{obs}$ values and their mean square errors defined as standard deviations $\sigma_{\bar{q}_{obs}}$ and $\sigma_{\bar{u}_{obs}}$ were derived.

To determine the instrumental polarization, the nearest unpolarized stars with a degree of polarization within the range from 0.00% to 0.04% with different positional angles, taken from the lists (Serkowsky 1974; Hsu & Breger 1982; Turnshek et al. 1990; Schmidt et al. 1992; Koch & Clarke 2005), were initially used. However, since the instrumental polarization was insignificant, $\sim$0.04%, we started

Table 1
Normalized Stokes Parameters q_{ins} and u_{ins} of the Instrumental Polarization and Zero-points of the Position Angle θ_{ins} of the Polarization Plane Measured with the CrAO and Terskol Polarimeters

CrAO Polarimeter				Terskol Polarimeter			
Band	$q_{ins} \pm \sigma_{q_{ins}}$ (%)	$u_{ins} \pm \sigma_{u_{ins}}$ (%)	$\theta_{ins} \pm \sigma_{P_{ins}}$ (deg)	Band	$q_{ins} \pm \sigma_{q_{ins}}$ (%)	$u_{ins} \pm \sigma_{u_{ins}}$ (%)	$\theta_{ins} \pm \sigma_{P_{ins}}$ (deg)
"Red" channel				"Red" channel			
R	-0.010 ± 0.007	0.020 ± 0.007	90.9 ± 1.0	R	0.012 ± 0.008	0.010 ± 0.013	95.8 ± 0.6
I	-0.014 ± 0.008	0.021 ± 0.012	95.1 ± 1.0	I	0.010 ± 0.007	0.006 ± 0.011	100.6 ± 0.7
"Blue" channel				"Blue" channel			
B	0.025 ± 0.006	-0.050 ± 0.006	0.9 ± 1.0	B	-0.001 ± 0.013	0.011 ± 0.009	11.3 ± 0.5
V	0.011 ± 0.011	-0.017 ± 0.025	-0.5 ± 1.0	V	0.004 ± 0.006	0.008 ± 0.009	5.4 ± 0.5

to use stars with strictly zero polarization ($P < 0.01\%$) from Serkowsky ([1974](#)). As a result of the observations of polarization standards, the average instrumental polarization parameters $\bar{q}_{ins}$ and $\bar{u}_{ins}$ and their mean square errors $\sigma_{\bar{q}_{ins}}$ and $\sigma_{\bar{u}_{ins}}$ were obtained for each season of observations. Two examples of the measurements of the instrumentation polarization are presented in Table [1](#).

The values of the instrumental Stokes parameters turned out to be small ($< 0.05\%$); however, a small temporal variability of the instrumental polarization parameters at a level of $\sim 0.02\%$ was found for different sets of observations. They were taken into account according to the expressions $q = \bar{q}_{obs} - \bar{q}_{ins}$ and $u = \bar{u}_{obs} - \bar{u}_{ins}$ for each observation run. The uncertainties in q and u were estimated according to the equations

$$\sigma_q = \sqrt{\sigma_{\bar{q}_{obs}}^2 + \sigma_{\bar{q}_{ins}}^2}, \quad \sigma_u = \sqrt{\sigma_{\bar{u}_{obs}}^2 + \sigma_{\bar{u}_{ins}}^2}. \quad (2)$$

Then, the degree of polarization P and the position angle of the polarization plane θ of satellites were determined from the following expressions:

$$P = \sqrt{q^2 + u^2}; \quad \theta = 0.5 \arctan\frac{u}{q} + \Delta PA, \quad (3)$$

where ΔPA is the correction for zero-point of the instrumental position angle. The uncertainties in P were estimated according to Skalidis et al. ([2018](#)) as

$$\sigma_P = \sqrt{(q^2\sigma_q^2 + u^2\sigma_u^2)/(q^2 + u^2)}, \quad (4)$$

and the uncertainties in the position angle of the polarization plane θ as

$$\sigma_\theta = 28.65\sigma_P/P. \quad (5)$$

To determine the zero-points of the instrumental positional angle, polarization standards with a high degree of polarization taken from Bailey & Hough ([1982](#)), Hsu & Breger ([1982](#)), Turnshek et al. ([1990](#)), Schmidt et al. ([1992](#)), and Wolff et al. ([1996](#)) were observed. The values of the θ angles were stable from season to season with uncertainties of $\leqslant 2°$ for all filters and for each observation set. A comparison of the measured degree of polarization of standard stars with their catalog values showed that the polarization efficiency factor of our polarimeters is close to unity.

The corrected values P and θ were in turn converted into quantities with respect to the scattering plane as

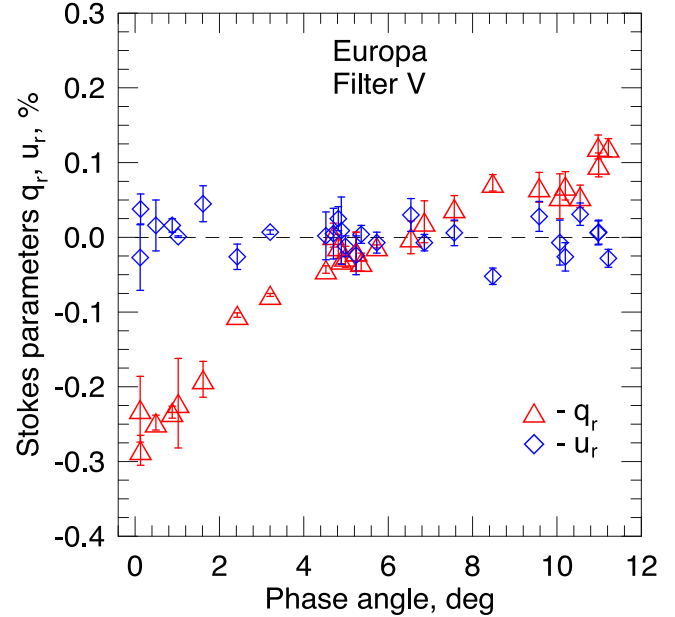$$P_r = q_r = P\cos 2\theta_r, \quad u_r = P\sin 2\theta_r, \quad \theta_r = \theta - (\vartheta \pm 90°), \quad (6)$$

Figure 1. Example of the phase-angle dependence of normalized Stokes parameters q_r and u_r for Europa in the V filter. The scatter of u_r values around zero characterizes the real observation errors.

where ϑ represents the position angle of the scattering plane, the sign of which ("$\pm$" in Equation ([6](#))) was chosen to satisfy $0 \leqslant \vartheta \pm 90° \leqslant 180°$ (Chernova et al. [1993](#)), and q_r and u_r are the Stokes parameters with respect to the scattering plane. As an example, Figure [1](#) presents the phase-angle dependence of normalized Stokes parameters q_r and u_r for Europa in the V filter. If there are no physical reasons and systematic errors in the angle θ, then the parameter u_r should be equal to θ within the observation errors in the polarization degree P. However, as Kiselev & Petrov ([2018](#)) have noted, when the measured polarization degree $P_{obs} \leqslant \sigma_{P_{obs}}$, the error in the observed position angle determined by Equation ([5](#)) becomes large and an additional error in $P_r = q_r$ and u_r can appear. Thus, the deviation of the u_r parameter from zero may be considered as an independent measure of a real accuracy of the q_r measurements. In our observations, they did not usually exceed 0.05% in the U and B filters and 0.02% in the V, R, and I filters.

3. Results of Observations

The results of polarization measurements of Europa are summarized in the Appendix (Table [4](#)). Figure [2](#) shows the phase-angle dependences of polarization for Europa in the
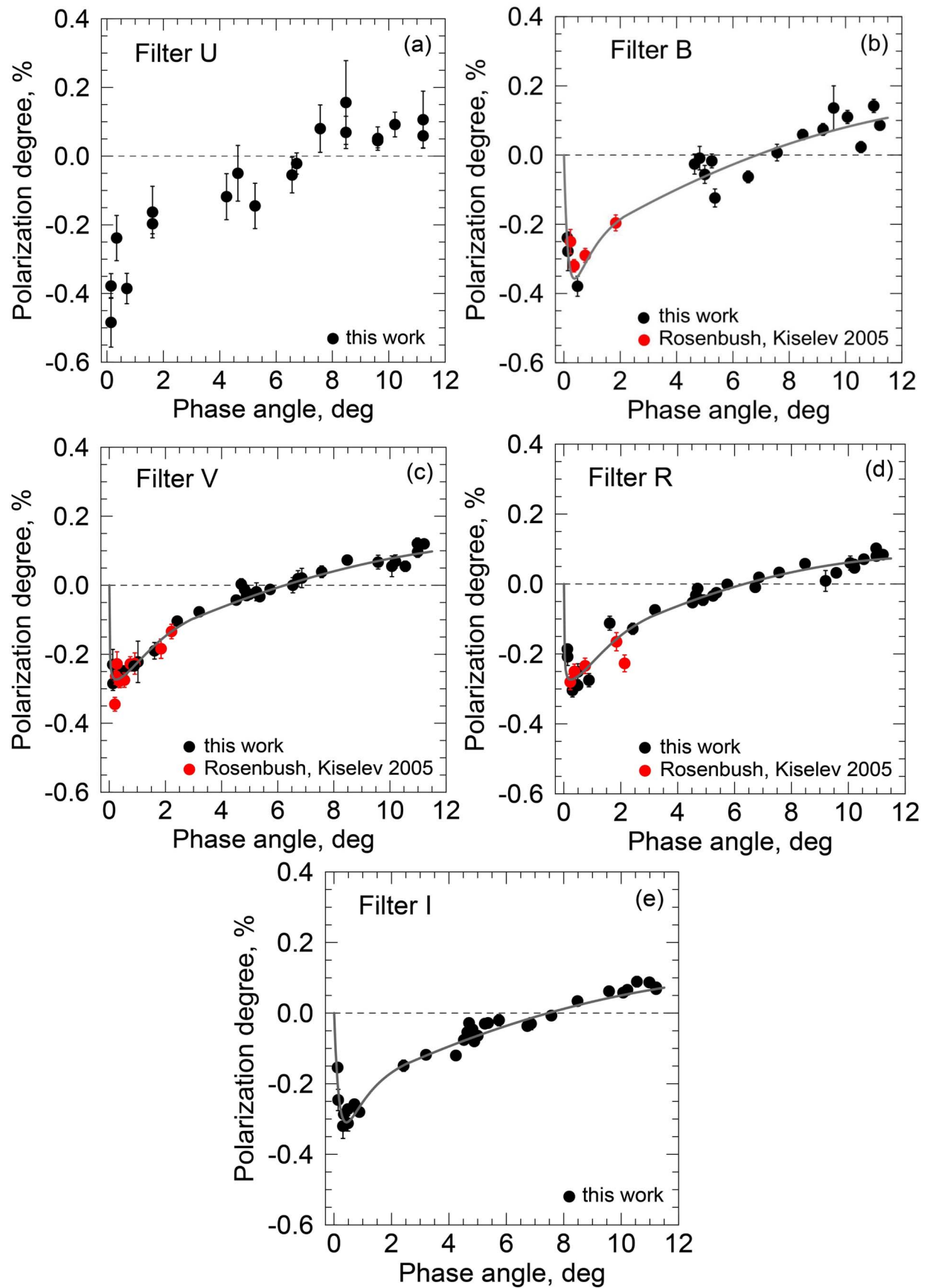
Figure 2. The phase-angle dependence of polarization for Europa in the *UBVRI* filters obtained in 2018–2021 (black circles) and in 2000 (Rosenbush & Kiselev 2005; red circles). The fit to the BVRI data showed by the solid curve consists of two parts: an approximation of data within the range of phase angles from 0° to ~3° and in the phase-angle range from approximately 3° to 12° using polynomials of the third and second degree, respectively.

Table 2
Parameters of the Negative Polarization Branch for Europa

Parameters	Band				
	U	B	V	R	I
α_{min} (deg)	∼0.14	0.45 ± 0.10	0.25 ± 0.10	0.39 ± 0.10	0.47 ± 0.10
P_{min} (%)	∼ − 0.43	-0.32 ± 0.03	-0.26 ± 0.03	-0.28 ± 0.03	-0.32 ± 0.03
α_{inv} (deg)	∼ 7.2 ± 0.8	7.0 ± 0.8	6.1 ± 0.8	6.2 ± 0.8	7.1 ± 0.8
h (% deg^{-1})	⋯	⋯	0.025 ± 0.003	⋯	⋯

UBVRI filters, which are combined with the results of polarization measurements of Europa in the *BVR* filters by Rosenbush & Kiselev ([2005](#)), close in accuracy to the present observations. As one can see, the polarization curves for Europa in all filters are represented by a curve with a sharp and deep minimum of the negative polarization at very small phase angles. To find the parameters α_{min} and P_{min} of the NPB for Europa in the *UBVRI* filters, we used an inverse polynomial of the third degree ($P(\alpha) = - \alpha/(A + B\alpha + C\alpha^2 + D\alpha^3)$) to fit the observation data within the range of phase angles approximately $0° - 3°$. The inversion angles α_{inv} and the polarimetric slope h were determined from an approximation of the data by a second-degree polynomial within the range of phase angles about $3° - 12°$. In Figure [2](#), the fit to the observational data is displayed by the solid curve. The obtained NPB parameters are given in Table [2](#). Because of a small number of observations and the large scatter of data points, the parameters P_{min}, α_{min}, and α_{inv} in the *U* filter were estimated manually. Due to the large scatter of data in a very small range of phase angles near the backward-scattering direction ($0° - 2°$), the spectral dependence of the parameters P_{min} and α_{min} cannot be determined reliably; however, it looks as though our observational data do not show strong dependence of the NPB parameters on the wavelength within the error limits in the visible domain.

It is extremely difficult to obtain full phase and spectral dependences of brightness and polarization for different longitudes from ground-based observations. This is because of geometrical constraints caused by the limitations of achievable phase angles and the rare occurrence of suitable satellite configurations for the observations. The study of brightness and polarization variations over the satellite surface requires long-term observations in order to make the measurements within each range of phase angles for the maximum possible range of longitudes. Therefore, the data are usually provided for the hemispheres of the satellite. For example, Thompson & Lockwood ([1992](#)) detected a very strong opposition spike in the brightness for both hemispheres of Europa at phase angles of less than 1° and concluded that the phase functions of brightness of the leading and trailing hemispheres of Europa are essentially indistinguishable over the range of accessible phase angles. However, the trailing hemisphere of Europa exhibits no detectable color change with phase angle, whereas the leading one clearly becomes bluer as the phase angle decreases. We also separated polarization data for the leading and trailing hemispheres to search for differences in polarization of the two hemispheres of Europa. Figure [3](#) shows the polarization for the leading ($0° < L < 180°$; filled circles) and trailing ($180° < L < 360°$; open circles) hemispheres of Europa in the *VRI* bands within the range of phase angles 4°–12°. The data for the *U* and *B* bands are sparse

and less accurate. As one can see in the figure, there is an insignificant difference (on average ∼0.02%) in the polarization degree between both hemispheres of Europa only in the *R* band: the polarization is systematically lower for the leading hemisphere. Most likely, the longitude effect, if it exists, is small, but this requires verification by additional observations.

Thus, the obtained data allow us to conclude the following: (i) The phase-angle curves of polarization for Europa in all filters are represented by a curve with a sharp minimum at very small phase angles. For the *BVRI* bands, $P_{min} \approx -0.3\%$ at phase angle $\alpha_{min} \leqslant 0°.4$, whereas in the *U* band, the polarization minimum is deeper, about -0.43% at $\alpha_{min} \approx 0°.2$. However, the depths and positions of the negative polarization minimum in the *U* filter need to be determined with additional accurate observations. (ii) After the minimum, the polarization gradually increases to positive values, passing the inversion point at the phase angle $\alpha_{inv} \approx 6° - 7°$. We have determined the polarimetric slope h at the inversion angle, which is $0.025\% \pm 0.003\%$ deg^{-1} in the *V* filter (Table [2](#)). According to the albedo−slope dependence $\log p_v = 1.016 \log h - 1.719$ (Lupishko [2018](#)), the geometric albedo of Europa in the *V* band is ∼0.8, which is close to the albedo 0.67 derived from photometry.

4. Modeling of the Results

Our knowledge on the surface of Europa, as well as other Galilean satellites, remains limited and fragmentary because of the lack of high-precision polarization measurements and because the light-scattering modeling for densely packed discrete media still faces serious fundamental problems (e.g., Tishkovets et al. [2011](#); Mishchenko et al. [2016](#) and references therein). There were numerous attempts to model the polarization of high-albedo bodies at small phase angles to reveal the characteristics of the regolith particles from the measurements of the negative polarization. Almost all computer or laboratory modeling showed that the high-albedo media exhibit a narrower and less deep negative branch of polarization. Laboratory measurements of layers formed by MgO (Lyot [1929](#)), Al_2O_3 (Geake & Geake [1990](#); Shkuratov et al. [2002](#)), or icy (Poch et al. [2018](#)) particles showed very asymmetric phase curves of polarization, which are similar to those we observed for Europa at phase angles $<3°$; however, at larger phase angles they demonstrated a very shallow NPB with the inversion point around 20°. The highly asymmetric NPB, observed for Europa and Saturn rings and for the high-albedo laboratory samples, has been explained using the coherent backscattering mechanism.

The scattering of electromagnetic waves by high-albedo discrete media of natural and artificial origin is accompanied by a narrow peak of intensity centered in the backscattering direction and a narrow branch of polarization near opposition.
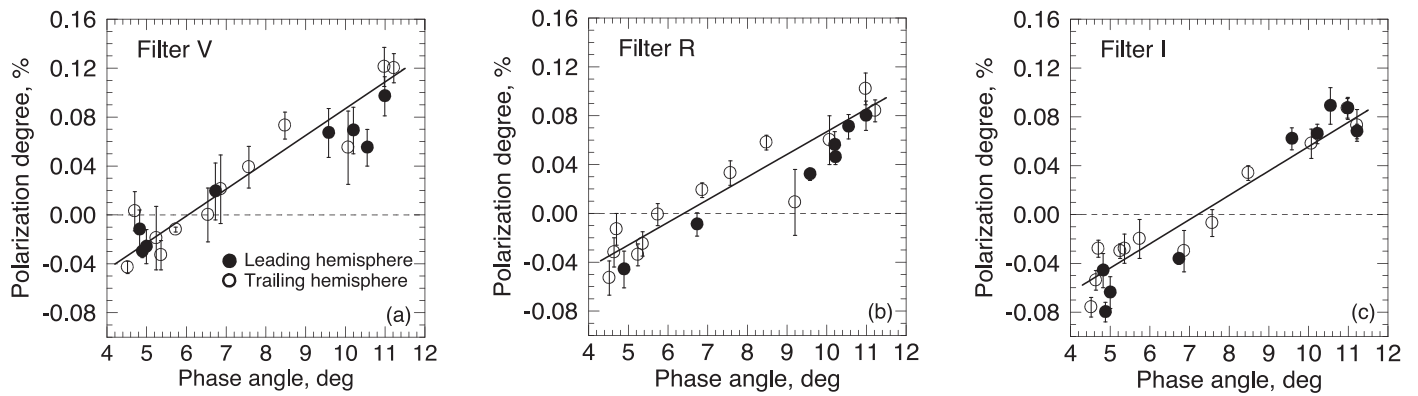
Figure 3. The phase-angle dependence of polarization for leading ($0° < L < 180°$; filled circles) and trailing ($180° < L < 360°$; open circles) hemispheres of Europa in the V, R, and I bands (left, middle, and right, respectively). The black lines are the linear fit to the trailing hemisphere data.

Table 3
Physical and Model Parameters

Parameters (Symbol)	Value
Single-scattering albedo (ω)	0.985
Parameters of double Henyey–Greenstein function (g, g_1, g_2)	$g = 0.6$, $g_1 = 0.8$, $g_2 = -0.1$
Maximum of polarization degree for the case of single scattering (p_{max})	0.08
Number of rays used in the Monte Carlo modeling (N)	10^7
Mean free path lengths (kl)	100, 150, 200

This phenomenon is caused by the interference of the reciprocal (having the same optical path but in the opposite direction) rays. The interference nature of the coherent backscattering makes the opposition effects dependent on the medium properties, specifically on size, refractive index, shape, and packing density of the scatterers in the medium.

The radiation scattered by the discrete random medium can be represented by a diffuse component that can be considered within the frames of the radiative transfer theory supplemented by coherent backscattering. For light scattering by particles beyond the Rayleigh regime, a computational approach of accounting for coherent backscattering in discrete random media was developed by Muinonen (2004). That was extended to parameterized, phenomenological scatterers by Muinonen & Videen (2012; see also Muinonen et al. 2015). The method is based on the RT-CB method. For different input parameters of the phenomenological model, listed below, the model can produce a variety of shapes of the NPB, from the polarization curves similar to those measured in the laboratory (e.g., MgO and Al_2O_3) to those observed by us for Europa.

The method developed by Muinonen & Videen (2012) considers light scattering by a medium consisting of particles that define single scattering. The properties of the particles are constrained phenomenologically through single-scattering albedo ω and maximum degree of linear polarization for the case of single scattering by regolith surface p_{max}. A single-scattering phase function is represented by a double Henyey–Greenstein function defined by the parameters g, g_1 and g_2.[7]

The radiative transfer computations were performed using the Monte Carlo method. Ray-tracing within the medium considers exponential extinction using the mean free path of

rays in the homogeneous and nonabsorbing medium, described by the size parameter kl, where k is the wavenumber $2\pi/\lambda$ and l is the extinction mean free path length in the scattering medium. The forward path of interactions corresponds to radiative transfer, and the forward and reciprocal paths together, via interference, give the coherent backscattering contribution. All small grains, populating a scattering volume mimicking the entire Europa, have the same scattering characteristics. The numerical values of the parameters of our model, ω, p_{max}, g, g_1, and g_2, are given in Table 3. For the scattering volume, the parameters result in the same geometric albedo $\rho = 0.67$ measured for Europa. The number of rays used in the Monte Carlo modeling was 10^7.

The best-fit modeling results are shown in Figure 4(a). There are model phase functions of polarization for three cases: $kl = 100$, 150, and 200. It should be noted that for larger kl the inversion angle shifts toward smaller values. The observations show that, within the observation accuracy, the inversion angle does not depend strongly on the wavelength in the visible range (see Table 2). The weak dependence on the wavelength can be explained by the self-similarity (fractal characteristics) of the Europa surface structure across the distance scales set by the present wavelengths, resulting in a change of extinction mean free path so that kl remains unchanged. Figure 4(b) illustrates the comparison of the observational data in the R filter with the best-fit modeling result to these data for $kl = 150$. Within the errors, the theoretical curve describes quite well the negative branch of polarization, whereas it goes slightly higher than the positive branch of polarization.

5. Discussion: The NPB Shape

A narrow backscattering intensity peak and an NPB have been detected for many ASSBs (see, e.g., Rosenbush & Mishchenko 2011), as well as particulate laboratory samples

---

[7] Here g is the total asymmetry parameter, and g_1 and g_2 are the asymmetry parameters of the two components. Here the total g fixes the weights of the component; see Muinonen et al. (2012).
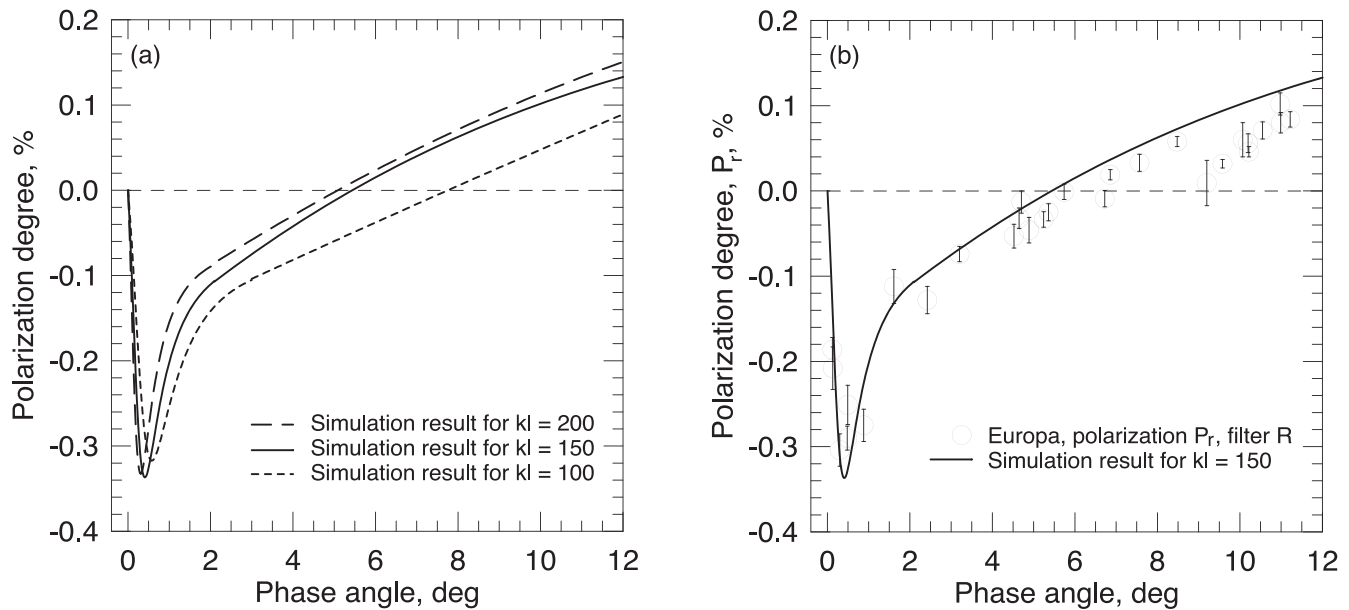
Figure 4. (a) Shifting the inversion point with increase of *kl*. (b) The best fit to the observational data in the *R* filter.

(Lyot 1929; Geake & Geake 1990; Shkuratov et al. 2002). Numerous observations demonstrate that the phase curve of negative polarization changes its shape and, accordingly, the parameters, for different composition, structure, and porosity of the surface. For low-albedo surfaces (e.g., asteroids), the polarization curve has almost parabolic shape with a minimum at phase angles between $\sim 5°$ and $\sim 15°$ and inversion point located between $\sim 15°$ and $\sim 30°$, depending on the taxonomical type (Belskaya et al. 2017). However, for icy surfaces (e.g., some satellites of the outer planets and their rings, trans-Neptunian objects) the NPB becomes very asymmetric, and its minimum shifts to smaller phase angles (Lyot 1929; Johnson et al. 1980; Bagnulo et al. 2006; Belskaya et al. 2010; Afanasiev et al. 2014). The NPB shape depends on the physical properties of the surface, in particular, on the size of the scattering particles. As Geake & Geake (1990) showed, the shape of the NPB for aluminum oxide (Al_2O_3) powder varies significantly from slightly parabolic for the 40 μm size particles to a very asymmetric curve with a deep minimum of the negative polarization near opposition for the 0.05 μm particles. The inversion angle does not change monotonically: it first increases and then decreases with decreasing particle size. As laboratory experiments have shown (Shkuratov et al. 2002), the shape of the NPB also depends on the degree of compression of the samples and even on the surface tilt.

To find out the reason for the discrepancy between the previous bimodal shape of the NPB (Rosenbush et al. 1997) and a single-modal very asymmetric curve of polarization obtained from our new observations (Figure 2), we studied the data by Dollfus (1975), part of which were obtained with an accuracy of better than ±0.03% and with a scatter of measurements smaller than 0.04%. In Figure 5(a), we present the measurements of polarization of Europa obtained by Dollfus (1975) and his approximation of these data by a second-degree polynomial (solid curve). In Figure 5(b), we compared the Dollfus data (blue circles) with our new polarimetric measurements (black circles) and the data obtained by Rosenbush & Kiselev (2005) (red circles) and

Zaitsev (2016) (green circles). Obviously, the data of Dollfus are in a very good agreement with ours, although there is a fairly large scatter of data, much more than in ours, and small systematic shift (see Figure 5(b)). Similar systematic shift in the Dollfus measurements was found for Callisto in the *V* filter by Rosenbush et al. (2002). Apparently, having no measurements of polarization at phase angles less than 2°, Dollfus tried to fit the conventional parabolic phase-angle dependences of polarization, typical for asteroids and the Moon from Lyot (1934).

Rosenbush et al. (1997) made their conclusion on a bimodal shape of the NPB of the high-albedo satellites of Jupiter on the basis of analysis of all results of measurements for the polarization near opposition of different ASSBs known at that time (Lyot 1929; Dollfus 1979; Johnson et al. 1980; Dollfus 1984 (see private communication in Rosenbush et al. 1997); Lupishko et al. 1994), laboratory samples (Lyot 1929; Geake & Geake 1990), and the theoretical studies by Mishchenko (1993). Later for the analysis, we added measurements of polarization of the Galilean satellites obtained during 2000–2011 by Rosenbush & Kiselev (2005), Kiselev et al. (2009), Zaitsev et al. (2012a), and Zaitsev et al. (2012b). The data of different authors at phase angles larger than 2°, including the previous data, were characterized by a significant scatter of data points. Their averaging within the range of 1° led to the conclusion that the phase function of polarization for Europa consists of a rather strong and extremely narrow opposition minimum of negative polarization at very small phase angles and a regular, almost flat branch of negative polarization (Rosenbush et al. 2015).

The simultaneous presence of the pronounced and very narrow BOE and POE for the high-albedo objects suggests that a significant fraction of their surfaces are covered by the fine-grained material, causing strong coherent backscattering. However, different parts of the icy surfaces of satellites can be covered by grains of different size and not only pure water ice, containing some amounts of various mineral and organic compounds. Therefore, it cannot be ruled out that the
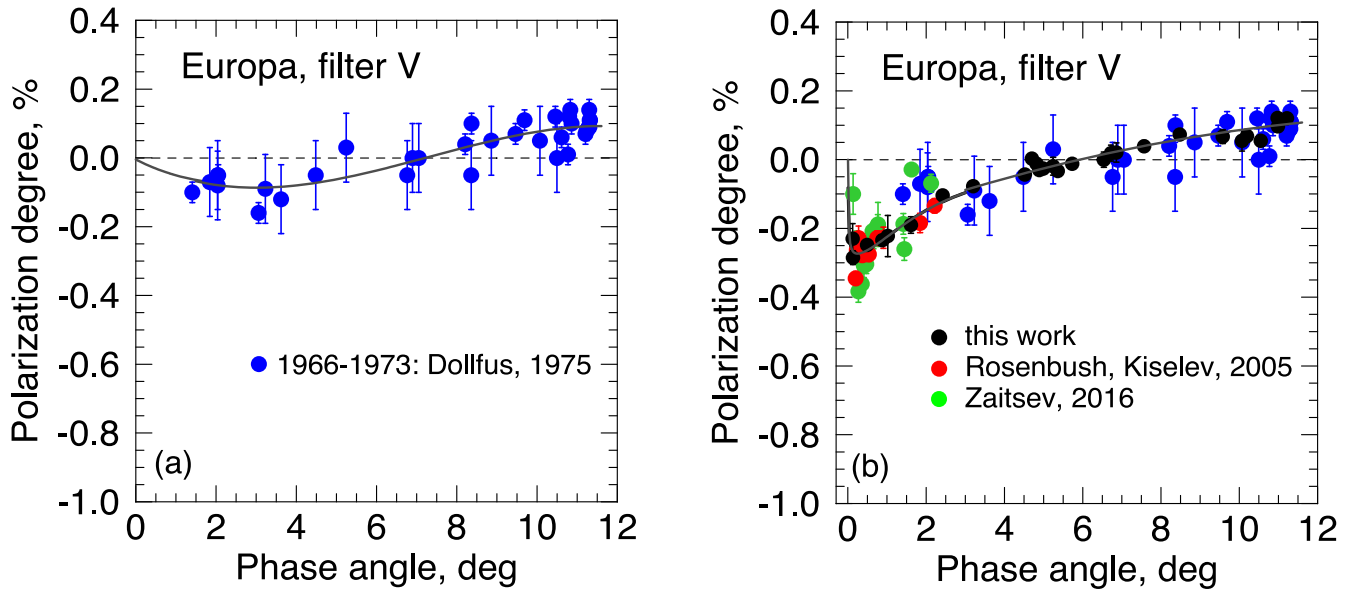
Figure 5. (a) Original data for Europa and the fit to them by a second-degree polynomial (blue curve) obtained by Dollfus (1975). (b) Comparison of the Dollfus data (blue circles) with our new polarimetric measurements (black circles) and the data obtained by Rosenbush & Kiselev (2005) (red circles) and Zaitsev (2016) (green circles). The fit to our data is displayed by the solid gray curve.

coherent backscattering negative polarization peak produced by the smallest grains can be superposed on the regular NPB produced by larger grains. Depending on the values of the parameters α_{min} and P_{min}, which specify the shape of the regular NPB and the peak of negative polarization, the resulting polarization curve can have different shapes at small phase angles: from two well-separated negative polarization minima to the extremely narrow minimum at phase angle close to 0°. This is exactly what modeling shows (see Figure 7 in Muinonen et al. 2015): when changing the input parameters, one can derive a parabolic curve or a curve with a narrow minimum. At present, only observations of asteroids (64) Angelina and (44) Nysa (Rosenbush et al. 2005; Rosenbush et al. 2009) indicate a bimodal NPB. But it is highly desirable to make new polarimetric observations of these asteroids with a high accuracy to determine the shape of the NPB.

6. Conclusions

In this study, we present our high-precision polarimetric observations of the Galilean satellite Europa carried out during the period 2018–2021 within the range of phase angles 0°.12–11°.2 accessible from Earth. For this, we used two telescopes, the 2.6 m telescope of the CrAO and the 2 m telescope at the Peak Terskol Observatory, which are equipped with identical two-channel photoelectric polarimeters "POLSHAKH" and the *UBVRI* filters.

In addition to characterizing the shape of the phase curve of polarization for Europa with high precision, we conducted computer modeling with the RT-CB technique to derive characteristics of the ice regolith. Our summary is the following:

1. The most accurate shape of the negative branch of polarization for Jupiter's moon Europa in the *UBVRI* bands is established. The observed NPB for Europa is represented as a sharp asymmetric curve with a single minimum $P_{min} \approx -0.3\%$ at phase angle $\alpha_{min} \leqslant 0°.4$.

After the minimum, the negative polarization decreases, reaching the inversion point between 6° and 7°. Within the error limits, the parameters P_{min}, α_{min}, and α_{inv} of the NPB are independent of the wavelength in the visible domain. The morphological profiles are qualitatively consistent with theoretical studies of the angular profile of the polarization opposition effect (Mishchenko 1993; Mishchenko et al. 2000, 2006, 2009; Muinonen et al. 2012; Muinonen & Videen 2012) and laboratory measurements of the polarization of different high-albedo samples, e.g., MgO, Al_2O_3, or water ice (Lyot 1929; Geake & Geake 1990; Shkuratov et al. 2002; Nelson et al. 2018; Poch et al. 2018).

2. We did not find a clearly pronounced longitude dependence of polarization for Europa. There is an insignificant difference (on average ~0.02%) in the polarization degree between the leading and trailing hemispheres of Europa only in the *R* band: the polarization is systematically lower for the leading hemisphere. Obviously, the longitude effect, if it exists, is small and requires verification by additional observations.

3. The computer modeling of the observed polarization curve based on RT-CB method, developed by Muinonen (2004) and Muinonen & Videen (2012), showed that the model curve reproduces well enough the observational asymmetric curve with a pronounced and narrow POE. The modeling also reproduces the observed geometric albedo of Europa. Future studies are directed toward a synoptic modeling of the brightness opposition effect and POE, as well as the physical interpretation of the resulting phenomenological model.

7. Perspectives

The surfaces of the icy satellites of the giant planets are affected by endogenous (tectonic activity and cryovolcanism) and exogenous (radiolysis and sputtering due to energetic

particles) processes responsible for changing the surface microtexture globally or locally (Poch et al. 2018, and references therein). Since the polarization is very sensitive to the size and structure of icy particles and porosity of the scattering medium, imaging polarimetry could be used to detect the areas affected by active processes on icy surfaces of satellites. Polarimetric observations at longer wavelengths should extend the polarization opposition effect to larger phase angles. This could provide more detailed information about icy surfaces.

Appendix
Results of Europa Polarimetry

Table 4 presents the measurements of polarization of Europa. These are the middle time of the observation UT; the phase angle α; the longitude L of the central meridian of Europa; the position angle of the scattering plane ϑ; the nightly average degree of polarization P and the position angle θ of the polarization plane with their mean square errors σ_P and σ_ϑ, respectively, in the equatorial plane; the position angle θ_r; and the degree P_r of polarization with respect to the scattering plane.

Table 4
Results of Polarimetric Observations of Europa in the *UBVRI* Filter

Observation Date (Y-M-D) (UT)	α (deg)	L (deg)	ϑ (deg)	$P \pm \sigma_P$ (%)	$\theta \pm \sigma_\theta$ (deg)	θ_r (deg)	P_r (%)
				U Filter			
2020-5-19.011	9.61	298.65	259.01	0.082 ± 0.034	143.21 ± 11.95	154.2	0.051
2020-5-19.011	9.61	298.65	259.01	0.053 ± 0.021	153.05 ± 11.68	164.04	0.045
2020-5-29.024	8.48	234.04	259.19	0.16 ± 0.142	162.85 ± 25.44	173.66	0.156
2020-5-29.024	8.48	234.04	259.19	0.181 ± 0.047	135.41 ± 7.48	146.22	0.069
2020-6-11.015	6.57	111.88	259.62	0.096 ± 0.052	52.12 ± 15.63	62.51	−0.055
2020-7-14.905	0.14	311.45	54.57	0.488 ± 0.072	50.50 ± 4.21	85.94	−0.484
2020-7-14.905	0.14	311.45	54.57	0.378 ± 0.036	55.09 ± 2.72	90.53	−0.378
2020-7-21.878	1.61	299.22	78.72	0.167 ± 0.075	72.04 ± 12.91	83.32	−0.163
2020-7-21.876	1.61	299.01	78.72	0.204 ± 0.029	85.91 ± 4.04	97.19	−0.197
2020-8-22.847	7.57	303.25	81.99	0.107 ± 0.069	12.53 ± 18.53	20.54	0.08
2020-9-14.749	10.22	105.38	82.48	0.095 ± 0.036	164.69 ± 10.76	172.2	0.092
2020-10-11.724	11.22	318.52	82.19	0.108 ± 0.083	166.21 ± 22.00	174.02	0.106
2020-10-12.688	11.22	56.06	82.13	0.104 ± 0.035	19.94 ± 9.59	27.81	0.059
2021-7-18.006	6.73	148.79	250.73	0.085 ± 0.031	73.53 ± 10.48	127.69	−0.021
2021-8-16.992	0.7	312.18	269.84	0.391 ± 0.044	85.30 ± 3.24	85.45	−0.386
2021-8-18.990	0.34	154.91	295.94	0.248 ± 0.066	107.72 ± 7.59	81.79	−0.238
2021-9-8.888	4.24	116.05	67.44	0.118 ± 0.067	64.42 ± 16.32	86.97	−0.118
2021-9-10.822	4.64	312.35	67.81	0.129 ± 0.081	101.26 ± 18.11	123.44	−0.05
2021-9-13.871	5.25	261.8	68.26	0.145 ± 0.066	66.53 ± 12.94	88.26	−0.145
				B Filter			
2019-3-3.132	10.55	76.38	273.59	0.090 ± 0.016	142.71 ± 4.92	37.6	0.023
2019-4-06.047	10.07	272.75	272.34	0.113 ± 0.019	8.85 ± 4.78	6.51	0.11
2019-6-10.890	0.12	112.69	163.72	0.239 ± 0.013	164.21 ± 1.56	90.49	−0.239
2019-6-12.915	0.48	318.26	107.59	0.379 ± 0.029	107.44 ± 2.20	89.85	−0.379
2019-7-04.876	4.82	27.2	96.88	0.043 ± 0.034	136.10 ± 22.38	129.22	−0.009
2019-7-5.811	5	122.02	96.87	0.076 ± 0.026	118.21 ± 9.72	111.34	−0.056
2019-7-7.804	5.36	324.34	96.88	0.127 ± 0.026	102.87 ± 5.77	95.99	−0.124
2019-7-14.800	6.54	309.85	96.89	0.087 ± 0.017	118.85 ± 5.69	111.95	−0.063
2020-5-29.011	8.48	232.77	259.19	0.069 ± 0.015	152.98 ± 6.21	163.79	0.059
2020-7-14.886	0.14	309.5	53.91	0.282 ± 0.056	48.92 ± 5.66	85.01	−0.278
2020-8-22.838	7.57	302.34	81.99	0.035 ± 0.024	133.04 ± 19.31	141.05	0.007
2020-9-7.748	9.58	115.63	82.41	0.137 ± 0.064	169.94 ± 13.45	177.53	0.136
2020-10-11.710	11.22	317.04	82.19	0.086 ± 0.012	173.38 ± 3.92	1.19	0.086
2020-10-23.685	11	89.56	81.73	0.144 ± 0.019	154.63 ± 14.31	174.54	0.142
2021-9-10.821	4.64	312.35	67.81	0.036 ± 0.029	45.33 ± 22.87	67.52	−0.026
2021-9-13.883	5.25	263.07	68.27	0.02 ± 0.02	84.59 ± 28.37	106.32	−0.017
2021-10-8.831	9.2	273.66	70.14	0.074 ± 0.017	159.89 ± 6.49	179.76	0.074
				V Filter			
2018-4-14.031	4.89	113.53	282.67	0.031 ± 0.005	94.32 ± 4.57	81.65	−0.030
2018-4-15.012	4.7	213.19	282.59	0.006 ± 0.016	42.11 ± 78.61	29.52	0.003
2018-4-15.987	4.52	312.07	282.51	0.043 ± 0.005	101.18 ± 3.33	88.67	−0.043
2018-5-4.960	0.88	77.71	270.16	0.235 ± 0.008	88.20 ± 0.98	88.04	−0.234
2018-5-6.915	0.49	276.32	256.5	0.249 ± 0.010	74.65 ± 1.15	88.15	−0.248
2018-5-13.877	1.02	262.89	119.4	0.222 ± 0.060	119.27 ± 7.74	89.87	−0.222
2018-5-20.889	2.42	254.64	111.88	0.107 ± 0.003	118.90 ± 0.80	97.02	−0.104
2018-5-24.897	3.2	301.38	110.58	0.077 ± 0.002	107.98 ± 0.74	87.4	−0.077
2018-6-7.821	5.73	274.38	108.95	0.014 ± 0.002	124.08 ± 4.12	105.13	−0.012
2018-6-14.845	6.86	266.94	108.64	0.022 ± 0.028	9.42 ± 36.24	−9.22	0.021
2019-3-3.117	10.55	74.91	273.59	0.064 ± 0.015	18.43 ± 6.67	14.84	0.055
2019-4-4.023	10.2	67.46	272.33	0.074 ± 0.019	171.79 ± 7.37	−10.51	0.069
2019-4-6.035	10.07	271.49	272.34	0.130 ± 0.023	169.07 ± 5.02	166.73	0.115
2019-6-10.890	0.12	112.69	163.72	0.232 ± 0.044	167.09 ± 5.49	93.37	−0.230
2019-7-4.873	4.82	26.77	96.88	0.028 ± 0.016	65.51 ± 16.54	58.63	−0.012
2019-7-5.805	4.99	121.39	96.87	0.030 ± 0.014	109.41 ± 13.51	102.54	−0.026
2019-7-7.788	5.36	322.65	96.88	0.034 ± 0.012	92.83 ± 10.26	85.95	−0.033
2019-7-14.745	6.54	308.51	96.89	0.029 ± 0.022	52.39 ± 21.88	45.5	0
2019-9-2.756	10.98	338.11	96.43	0.121 ± 0.016	7.73 ± 3.80	1.3	0.121
2019-9-3.715	10.99	78.56	96.37	0.097 ± 0.016	8.52 ± 4.72	2.15	0.097
2020-5-28.984	8.48	230.02	259.19	0.090 ± 0.011	151.46 ± 3.58	162.27	0.073

Table 4
(Continued)

Observation Date (Y-M-D) (UT)	α (deg)	L (deg)	ϑ (deg)	$P \pm \sigma_P$ (%)	$\theta \pm \sigma_\theta$ (deg)	θ_r (deg)	P_r (%)
2020-7-14.872	0.13	308.14	53.4	0.288 ± 0.020	49.59 ± 2.02	86.2	−0.285
2020-7-21.861	1.61	297.53	78.72	0.195 ± 0.024	72.07 ± 3.52	83.35	−0.190
2020-8-22.832	7.57	301.7	81.99	0.039 ± 0.017	176.53 ± 12.51	4.54	0.039
2020-9-7.740	9.58	114.86	82.41	0.073 ± 0.020	3.64 ± 7.95	11.24	0.067
2020-10-11.696	11.22	315.64	82.19	0.123 ± 0.012	165.58 ± 2.84	173.39	0.12
2021-7-18.034	6.73	151.61	250.73	0.027 ± 0.023	3.18 ± 24.60	22.44	0.019
2021-9-13.859	5.24	260.61	68.26	0.031 ± 0.026	42.31 ± 24.05	64.05	−0.019
				R Filter			
2018-4-14.050	4.89	115.43	282.67	0.047 ± 0.015	97.37 ± 9.33	84.7	−0.046
2018-4-15.025	4.7	214.46	282.59	0.016 ± 0.013	85.36 ± 23.07	72.77	−0.013
2018-4-16.005	4.52	313.98	282.51	0.054 ± 0.014	98.86 ± 7.66	86.34	−0.053
2018-5-04.931	0.88	74.75	270.27	0.275 ± 0.019	89.87 ± 1.95	89.6	−0.275
2018-5-6.925	0.49	277.24	256.4	0.252 ± 0.023	77.24 ± 2.61	90.84	−0.251
2018-5-20.889	2.42	255.56	111.87	0.129 ± 0.016	109.84 ± 3.51	87.96	−0.128
2018-5-24.898	3.2	302.37	110.58	0.077 ± 0.009	102.69 ± 3.42	82.11	−0.074
2018-6-7.831	5.74	275.72	108.95	0.031 ± 0.009	64.50 ± 7.91	45.55	−0.001
2018-6-14.853	6.86	267.79	108.64	0.031 ± 0.006	44.60 ± 5.84	25.96	0.019
2019-3-3.117	10.55	74.91	273.59	0.073 ± 0.010	10.07 ± 3.92	6.48	0.071
2019-4-4.018	10.2	67.03	272.33	0.056 ± 0.011	2.79 ± 5.82	0.49	0.056
2019-4-6.029	10.07	272.34	272.34	0.080 ± 0.020	161.60 ± 5.70	159.26	0.06
2019-6-10.880	0.12	111.7	164.67	0.187 ± 0.014	162.76 ± 2.09	88.09	−0.186
2019-6-11.977	0.3	223.1	115.87	0.305 ± 0.019	114.63 ± 1.75	88.76	−0.304
2019-6-12.901	0.48	316.92	107.66	0.291 ± 0.014	107.86 ± 1.33	90.2	−0.290
2019-7-7.788	5.36	322.65	96.88	0.025 ± 0.010	95.39 ± 11.76	88.5	−0.025
2019-9-2.747	10.98	337.47	96.43	0.104 ± 0.013	3.91 ± 3.52	−2.52	0.102
2019-9-3.739	10.99	77.86	96.37	0.080 ± 0.012	5.07 ± 4.39	−1.30	0.08
2020-5-28.983	8.48	229.88	259.19	0.058 ± 0.006	168.25 ± 2.89	179.07	0.058
2020-7-14.872	0.13	308.14	53.4	0.214 ± 0.025	46.62 ± 3.40	83.23	−0.208
2020-7-21.861	1.61	297.53	78.72	0.112 ± 0.020	78.14 ± 5.26	89.42	−0.112
2020-8-22.832	7.57	301.7	81.99	0.035 ± 0.010	161.78 ± 8.08	169.78	0.033
2020-9-7.740	9.58	114.86	82.41	0.032 ± 0.005	169.63 ± 4.42	177.22	0.032
2020-9-14.743	10.22	104.75	82.48	0.052 ± 0.006	158.46 ± 3.08	165.98	0.046
2020-10-11.697	11.22	315.78	82.19	0.084 ± 0.009	175.74 ± 3.23	3.55	0.084
2021-7-18.034	6.73	151.61	250.73	0.016 ± 0.010	42.55 ± 16.78	61.82	−0.009
2021-9-10.822	4.64	312.35	67.81	0.032 ± 0.012	68.04 ± 10.81	90.22	−0.032
2021-9-13.859	5.24	260.61	68.26	0.036 ± 0.009	80.03 ± 7.14	101.77	−0.034
2021-10-8.830	9.2	273.67	70.14	0.034 ± 0.027	123.01 ± 22.17	142.86	0.009
				I Filter			
2018-4-14.067	4.88	117.19	282.66	0.083 ± 0.008	94.54 ± 2.78	81.89	−0.080
2018-4-15.045	4.7	216.58	282.59	0.028 ± 0.007	96.18 ± 7.14	83.59	−0.028
2018-4-16.025	4.52	316.02	282.51	0.076 ± 0.008	100.65 ± 2.96	88.14	−0.076
2018-5-04.949	0.88	76.51	270.2	0.282 ± 0.011	87.32 ± 1.14	87.12	−0.280
2018-5-6.941	0.48	278.93	256.2	0.272 ± 0.013	74.29 ± 1.36	88.09	−0.272
2018-5-20.911	2.42	256.9	111.87	0.151 ± 0.016	107.92 ± 3.00	86.06	−0.149
2018-5-24.924	3.2	304.13	110.57	0.125 ± 0.010	100.88 ± 2.28	80.31	−0.118
2018-6-7.849	5.74	277.2	108.95	0.023 ± 0.016	95.71 ± 20.54	76.76	−0.020
2018-6-14.868	6.86	269.34	108.63	0.035 ± 0.017	92.78 ± 14.05	74.15	−0.030
2019-3-3.132	10.55	76.38	273.59	0.094 ± 0.015	13.49 ± 4.63	9.9	0.089
2019-4-6.040	10.07	272.05	272.34	0.058 ± 0.012	5.73 ± 5.60	3.39	0.058
2019-6-10.890	0.12	112.69	163.72	0.156 ± 0.013	158.47 ± 2.46	84.75	−0.154
2019-6-11.996	0.31	225.08	115.58	0.320 ± 0.035	116.93 ± 3.17	91.35	−0.320
2019-6-12.915	0.48	318.26	107.59	0.312 ± 0.022	108.71 ± 2.05	91.12	−0.312
2019-7-4.880	4.82	28.46	96.88	0.053 ± 0.014	82.56 ± 7.45	75.68	−0.046
2019-7-5.818	5	122.66	96.87	0.065 ± 0.013	92.86 ± 5.75	85.99	−0.064
2019-7-7.805	5.36	324.41	96.88	0.028 ± 0.012	93.23 ± 12.67	86.35	−0.028
2019-9-2.761	10.98	338.95	96.43	0.087 ± 0.008	8.55 ± 2.83	2.12	0.087
2019-9-3.753	10.99	79.27	96.37	0.087 ± 0.009	5.93 ± 2.83	−0.44	0.087
2020-5-29.010	8.48	232.63	259.19	0.035 ± 0.006	174.27 ± 5.14	5.08	0.034
2020-7-14.886	0.14	309.5	53.9	0.251 ± 0.030	48.27 ± 3.45	84.37	−0.246
2020-8-22.843	7.57	302.83	81.99	0.021 ± 0.011	116.35 ± 15.03	124.35	−0.007
2020-9-7.749	9.58	115.77	82.41	0.062 ± 0.009	170.97 ± 4.18	178.56	0.062

Table 4
(Continued)

Observation Date (Y-M-D) (UT)	α (deg)	L (deg)	ϑ (deg)	$P \pm \sigma_P$ (%)	$\theta \pm \sigma_\theta$ (deg)	θ_r (deg)	P_r (%)
2020-9-14.755	10.22	105.94	82.48	0.066 ± 0.008	171.51 ± 3.30	179.03	0.066
2020-10-11.713	11.22	317.4	82.19	0.073 ± 0.013	169.50 ± 5.03	177.31	0.073
2020-10-12.689	11.22	56.13	82.13	0.073 ± 0.006	2.64 ± 2.28	10.51	0.068
2021-7-18.007	6.73	148.79	250.73	0.041 ± 0.004	57.36 ± 3.13	76.63	-0.036
2021-8-16.992	0.7	312.18	269.85	0.258 ± 0.007	90.24 ± 0.82	90.4	-0.258
2021-8-18.989	0.34	154.84	295.92	0.287 ± 0.011	117.36 ± 1.14	91.44	-0.286
2021-9-8.888	4.24	116.05	67.44	0.12 ± 0.008	67.19 ± 1.86	89.75	-0.12
2021-9-10.822	4.64	312.35	67.81	0.054 ± 0.008	64.6 ± 4.37	86.78	-0.054
2021-9-13.875	5.25	262.22	68.26	0.034 ± 0.006	82.67 ± 5.11	104.41	-0.03

ORCID iDs

Nikolai Kiselev ⬤ https://orcid.org/0000-0002-2451-4079
Ludmilla Kolokolova ⬤ https://orcid.org/0000-0002-9321-3202

References

Afanasiev, V. L., Rosenbush, V. K., & Kiselev, N. N. 2014, AstBu, 69, 211
Bagnulo, S., Belskaya, I. N., Boehnhardt, H., et al. 2011, JQSRT, 112, 2059
Bagnulo, S., Boehnhardt, H., Muinonen, K., et al. 2006, A&A, 450, 1239
Bailey, J., & Hough, J. H. 1982, PASP, 94, 618
Belskaya, I. N., Bagnulo, S., Barucci, M. A., et al. 2010, Icar, 210, 472
Belskaya, I. N., Fornasier, S., & Tozzi, G. P. 2017, Icar, 284, 30
Bolkvadze, O. R. 1981, in Proc. of the Third Finnish-Soviet Astronomical Symp. 73 (Helsinki: Astronomical Society of Finland)
Botvinova, V. V., & Kucherov, V. A. 1980, AAfz, 41, 59
Cassen, P., Reynolds, R. T., & Peale, S. J. 1979, GeoRL, 6, 731
Chernova, G. P., Kiselev, N. N., & Jockers, K. 1993, Icar, 103, 144
Chigladze, R. A. 1989, PhDT, Abastumany Astrophys. Obs., Georgia
Dollfus, A. 1975, Icar, 25, 416
Dollfus, A. 1979, Icar, 37, 404
Dollfus, A. 1984, in Anneaux de Planétes, ed. A. Brahic (Tolouse: CNRS), 121
Domingue, D. L., Hapke, B. W., Lockwood, G. W., & Thompson, D. T. 1991, Icar, 90, 30
Franklin, F. A., & Cook, A. F. 1965, AJ, 70, 704
Geake, J. E., & Geake, M. 1990, MNRAS, 245, 46
Gradie, J., & Zellner, B. 1973, BAAS, 5, 404
Helfenstein, P., Currier, N., Clark, B. E., et al. 1998, Icar, 135, 41
Hsu, J.-C., & Breger, M. 1982, ApJ, 262, 732
Johnson, P. E., Kemp, J. C., King, R., et al. 1980, Natur, 283, 146
Kiselev, N., & Petrov, D. 2018, SoSyR, 52, 282
Kiselev, N., Rosenbush, V., Velichko, F., & Zaitsev, S. 2009, JQSRT, 110, 1713
Kivelson, M. G., Khurana, K. K., Russell, Ch. T., et al. 2000, Sci, 289, 1340
Koch, R. H., & Clarke, D. 2005, Obs, 123, 355
Levasseur-Regourd, A. C., Renard, J.-B., & Shkuratov, Yu. 2015, in Polarimetry of Stars and Planetary Systems, ed. L. Kolokolova, J. Hough, & A. Ch. Levasseur-Regourd (Cambridge: Cambridge Univ. Press), 62
Lockwood, G. W. 1983, in Solar System Photometry Handbook, Vol. 2 ed. R. M. Genet (Richmond: Willmann-Bell), 1
Lupishko, D. F. 2018, SoSyR, 52, 98
Lupishko, D. F., Kiselev, N. N., Chernova, G. P., et al. 1994, KFNT, 10, 40
Lyot, B. 1929, Ann. Obs. Paris 8, No. 1, English transl. 1964, NASA TT F-187
Lyot, B. 1934, Comptes Rendus de l'Académie des Sciences, 199, 774
Markkanen, J., Väisänen, T., Penttilä, A., & Muinonen, K. 2018, OptL, 43, 2925
Mishchenko, M., Rosenbush, V., & Kiselev, N. 2006, ApOpt, 45, 4459
Mishchenko, M. I. 1993, ApJ, 411, 351
Mishchenko, M. I., Dlugach, J. M., Li, L., et al. 2009, ApJL, 705, L118
Mishchenko, M. I., Dlugach, J. M., Yurkin, M. A., et al. 2016, PhR, 632, 1
Mishchenko, M. I., Liu, L., Mackowski, D. W., et al. 2007, OExpr, 15, 2822
Mishchenko, M. I., Luck, J.-M., & Nieuwenhuizen, Th. M. 2000, JOSAA, 17, 888
Mishchenko, M. I., Rosenbush, V. K., Kiselev, N. N., et al. 2010, arXiv:1010.1171

Morozhenko, A. V. 2001, KFNT, 17, 45
Müeller, G. 1893, Pub. Ap. Obs. Potsdam, 8, 197
Muinonen, K. 1990, Light Scattering by Inhomogeneous Media: Backward Enhancement and Reversal of Linear Polarization (Helsinki: Univ. Helsinki)
Muinonen, K. 1994, in IAU Symp. 160, Asteroids, Comets, Meteors 1993, ed. A. Milani, M. Di Martino, & A. Cellino (Dordrecht: Kluwer), 271
Muinonen, K. 2004, WRM, 14, 365
Muinonen, K., Markkanen, J., Väisänen, T., et al. 2018, OptL, 43, 683
Muinonen, K., Mishchenko, M. I., Dlugach, J. M., et al. 2012, ApJ, 760, 118
Muinonen, K., Penttilä, A., & Videen, G. 2015, in Polarimetry of Stars and Planetary Systems, ed. L. Kolokolova, J. Hough, & A. C. Levasseur-Regourd (Cambridge: Cambridge Univ. Press), 114
Muinonen, K., & Videen, G. 2012, JQSRT, 113, 2385
Muinonen, K. O., Sihvola, A. H., Lindell, I. V., & Lumme, K. A. 1991, JOSAA, 8, 477
Nelson, R. M., Boryta, M. D., Hapke, B. W., et al. 2018, Icar, 302, 483
Paganini, L., Villanueva, G. L., Roth, L., et al. 2020, NatAs, 4, 266
Poch, O., Cerubini, R., Pommerol, A., et al. 2018, JGRE, 123, 2564
Rosenbush, V., Kiselev, N., & Afanasiev, V. 2015, in Polarimetry of Stars and Planetary Systems, ed. L. Kolokolova, J. Hough, & A. Ch. Levasseur-Regourd (Cambridge: Cambridge Univ. Press), 340
Rosenbush, V., Kiselev, N., Avramchuk, V., & Mishchenko, M. 2002, in Optics of Cosmic Dust, ed. G. Videen & M. Kocifaj (Dordrecht: Kluwer), 191
Rosenbush, V. K., Avramchuk, V. V., Rosenbush, A. E., & Mishchenko, M. I. 1997, ApJ, 487, 402
Rosenbush, V. K., & Kiselev, N. N. 2005, Icar, 179, 490
Rosenbush, V. K., Kiselev, N. N., & Shevchenko, V. G. 2005, Icar, 178, 222
Rosenbush, V. K., & Mishchenko, M. I. 2011, in Polarimetric Detection, Characterization, and Remote Sensing, ed. M. I. Mishchenko et al. (Berlin: Springer), 409
Rosenbush, V. K., Shevchenko, V. G., Kiselev, N. N., et al. 2009, Icar, 201, 655
Schmidt, G. D., Elston, R., & Lupie, O. L. 1992, AJ, 104, 1563
Serkowsky, K. 1974, in IAU Coll. Proc. 23, Planets, Stars, and Nebulae: Studied with Photopolarimetry, ed. T. Gehrels (Tucson, AZ: Univ. Arizona Press), 135
Shakhovskoy, D., Kiselev, N., Dolgopolov, A., et al. 2022, ExA, in press
Shkuratov, Y., Ovcharenko, A., Zubko, A., et al. 2002, Icar, 159, 396
Shkuratov, Yu. G. 1985, ATsir, 1400, 1
Shkuratov, Yu. G. 1991, SoSyR, 25, 110
Skalidis, R., Panopoulou, G. V., Tassis, K., et al. 2018, A&A, 616, A52
Sparks, W. B., Hand, K. P., McGrath, M. A., et al. 2016, ApJ, 829, 121
Sparks, W. B., Schmidt, B. E., McGrath, M. A., et al. 2017, ApJL, 839, L18
Thompson, D. T., & Lockwood, G. W. 1992, JGR, 97, 14761
Tishkovets, V. P., Petrova, E. V., & Mishchenko, M. I. 2011, JQSRT, 112, 2095
Turnshek, D. A., Bohlin, R. C., Williamson, R. L., II, et al. 1990, AJ, 99, 1243
Veverka, J. 1971, Icar, 14, 355
Veverka, J. 1977, in IAU Coll. Proc. 28, Planetary Satellites, ed. J. A. Burns (Tucson, AZ: Univ. Arizona Press), 210
von Seeliger, H. 1887, Abhandl. Bayer. Akad. Wiss., K1 II, 16, 405
Wolff, M. J., Nordsieck, K. H., & Nook, M. A. 1996, AJ, 111, 856
Zaitsev, S., Rosenbush, V., & Kiselev, N. 2012a, NASA Planetary Data System, id. EAR-SA-COMPIL-3-SATPOL-V1.0
Zaitsev, S. V. 2016, PhD thesis, Main Astronomical Observatory, Kyiv
Zaitsev, S. V., Kiselev, N. N., Rosenbush, V. K., et al. 2012b, AASP, 2, 177
Zimmer, C., Khurana, K., & Kivelson, M. G. 2000, Icar, 147, 329